SAR Image Change Detection Based on Nonlocal Low-Rank Model and Two-Level Clustering

Yuli Sun, Lin Lei, Dongdong Guan, Xiao Li, and Gangyao Kuang, *Senior Member, IEEE*

***Abstract*—Change detection (CD) has found a wide range of applications in many fields. In this article, we propose a novel nonlocal low-rank (NLR) based method for multitemporal synthetic aperture radar image CD. This method jointly exploits the powerful NLR-based despeckling and the effective cascade clustering. First, the NLR model is used to generate the difference image (DI), which consists of a patch grouping process and a low-rank minimizing process. Especially, the NLR minimization model contains a data fidelity term, which is based on the statistical distribution of speckle noise, and a regularization term, which uses the weighted nuclear norm. Then, the alternating direction methods of multipliers is introduced to solve this minimization problem. Second, after DI is generated, the principal component analysis is employed to extract the feature and a two-level clustering method is used to generate the final change map, which separates the intermediate class by using the neighbor information with Gaussian weighted distance. Experiment results demonstrate the effectiveness of the proposed method by comparing with some state-of-the-art methods.**

***Index Terms*—Low-rank modeling, speckle reduction, synthetic aperture radar (SAR) images, two-level clustering, unsupervised change detection (CD).**

I. Introduction

CHANGE detection (CD) is a process of identifying changes of an object or phenomenon that have occurred in the same geographical area at different times. In the field of synthetic aperture radar (SAR) image processing, CD is a very important topic, which has a wide range of applications in both civil and military domains, such as disaster relief, agricultural survey, urban planning, and military monitoring [1]–[3].

Generally, according to whether the label information is used, CD algorithms can be divided into three categories: the supervised [4], semisupervised [5], [6], and unsupervised [7], [8]. Although the supervised and semisupervised approaches can provide better performance theoretically, they usually need the ground truth or the labeled samples for training, which are difficult to obtain in some practical applications. Therefore, we focus on the unsupervised CD method to discriminate the changed and unchanged classes without requiring any ground reference.

The procedure of traditional unsupervised CD in SAR images can be divided into three steps: image preprocessing, difference image (DI) generation and analysis of the DI [9]. In the first step, geometric correction and registration are usually implemented to align two images into the same coordinate frame. In the second step, a DI is generated, which can initially discern the changed and unchanged areas. Then, the DI can be divided into two classes in the third step. Among them, the construction of DI has a close relationship with the result of CD. Generally, the methods of generating DI mainly include difference operator and ratio operator. However, the speckle noise in SAR images makes it more difficult to generate a clean DI for CD. To overcome this problem, the log-ratio operator [10], which can transform the multiplicative noise into additive noise is often used for its robustness and insensitivity to speckle noise. Furthermore, the ratio mean detector [11] based on the ratio of local intensity means of pixel patches can enhance the low-intensity pixels, which is also robust to speckle noise. There are some other works proposed recently to generate a better DI-based on the fusion of different methods, such as the wavelet fusion technique on both log-ratio and mean-ratio images [12]–[14], the wavelet fusion technique on Gauss-log ratio and log-ratio images [15], the saliency extraction guided log-ratio images [16], the shearlet fusion technique on saliency extraction, and Gauss-log ratio images [17]. Due to the presence of the speckle noise, it is difficult to keep tradeoff between robustness to noise and effectiveness of preserving the detail [18]. Although the ratio-based methods can partially reduce the impact of noise, they cannot make full use of multitemporal remote sensing images and there will still be some residual noise that would seriously affect the detection performance.

Recently, the nonlocal low-rank (NLR) model has attached much attention for its superior performance in denoising [19]–[21]. These methods first group similar patches within a local window, then assume that the patches in each group share similar underlying structure, which means that the patches stacked group matrix have a low-rank property. Then, low-rank minimization problem is modeled to reconstruct the clean image patches. The NLR model has also been extended to SAR image processing [22], [23] and brings effective performance. In this article, we introduce the NLR model to generate the DI, which can effectively utilize the characteristics of speckle noise, aiming to reduce the noise and provide better DI for CD. Instead of separately applying NLR to the original multitemporal images

Manuscript received June 14, 2019; revised September 15, 2019 and November 11, 2019; accepted December 11, 2019. Date of publication January 2, 2020; date of current version February 12, 2020. This work was supported in part by the National Natural Science Foundation of China (61701508). *(Corresponding author: Gangyao Kuang.)*

The authors are with the College of Electronic Science, National University of Defense Technology, Changsha 410073, China (e-mail: sunyuli@mail.ustc.edu.cn; alaleilin@163.com; guandd@hotmail.com; lxcherishm@126.com; kuangyeats@hotmail.com).

Digital Object Identifier 10.1109/JSTARS.2019.2960518

to obtain two independent denoising images, or simply applying NLR to the log-ratio DI directly, the proposed NLR model jointly uses the statistical distribution characteristics of the multitemporal images, which can avoid the loss of information in the subtraction process and lead to a better quantity of DI.

After the DI is obtained, the CD can be treated as an image binary segmentation problem. The clustering method is widely used for its simplicity and effectiveness, which is a process of grouping a set of features into meaningful clusters [24]. In order to extract the features, principal component analysis (PCA) [25], compressed projection [15], and Gabor wavelets [26] are often used. Then, the clustering methods, such as K-means clustering [27], fuzzy c-means (FCM) clustering [28], fuzzy local information c-means [29], Markov random field FCM (MRFFCM) [30] are often employed to obtain the final result. In this article, we employ the PCA to extract the feature vectors and modify the two-level clustering scheme proposed in [26] to identify the changed and unchanged classes by implementing FCM with the nearest neighbor rule with Gaussian weighted distance.

The main contributions of this article are twofold. First, we propose a speckle noise distribution based NLR model for generating DI. Especially, we modify the data fidelity term in the traditional NLR-based methods according to the noise characteristics of two original observed SAR images. To improve the performance, the weighted nuclear norm (WNM) [31] is employed for the rank minimization problem. Then, the alternating direction methods (ADM) of multipliers (ADMM) is used to solve the unconstrained optimization problem. Second, we modify the two-level clustering scheme to classify the PCA-extracted feature, which separates the intermediate classes by using the neighbors information with Gaussian weighted distance.

The remainder of this article is organized as follows. Section II presents the proposed NLR DI model based CD method. Section III shows the experimental results, and Section IV provides the conclusion.

II. Proposed CD Method

We consider two coregistered SAR intensity images $\mathbf{Y}_1 = \{y_1(i,j)|1 \le i \le I, 1 \le j \le I\}$ and $\mathbf{Y}_2 = \{y_2(i,j)|1 \le i \le I, 1 \le j \le I\}$, which are acquired on the same geographical area but at two different times. CD is aiming to generate a binary change map to classify the changed and unchanged class. The proposed method consists of three steps: 1) DI generation, which includes logarithmic images generation, patch construction, and low-rank recovery; 2) PCA feature extraction; and 3) modified two-level clustering, which includes the FCM and Gaussian weighted distance classification. The framework is illustrated in Fig. 1.

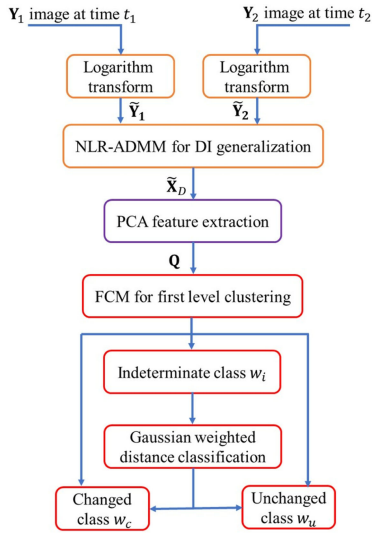

Fig. 1. Framework of the proposed CD method.

A. NLR Modeling for DI

Very recently, the NLR model has attracted researchers' attention on the SAR image despeckling [22], [23]. Here, we extend it to the SAR image CD. We first suppose that $\mathbf{X}_1$ and $\mathbf{X}_2$ are the underlying backscattering coefficients corresponding to $\mathbf{Y}_1$ and $\mathbf{Y}_2$, respectively. Then, $\mathbf{Y}$ is related to $\mathbf{X}$ by the well-accepted multiplicative model (dropping the pixel subscript for simplicity)

$$\mathbf{Y}_t = \mathbf{X}_t \mathbf{N}_t, \quad t = 1, 2 \tag{1}$$

where $\mathbf{N}$ is the corresponding speckle noise. The statistical properties of speckle have been widely studied and are the topic of a large body of literature, here we use the widely recognized and used Gamma distribution with unit mean [32]. The probability density function (pdf) of $\mathbf{N}$ is given by

$$p_{N_t}(N_t) = \frac{L_t^{L_t} N_t^{L_t - 1} e^{-L_t N_t}}{\Gamma(L_t)}, \; N_t \ge 0, \; L_t \ge 1, \; t = 1, 2 \tag{2}$$

where $\Gamma(\cdot)$ denotes the Gamma function, and L is the equivalent number of looks (ENL).

Applying the logarithmic transform to (1), an additive noise model is obtained

$$\tilde{\mathbf{Y}}_t = \tilde{\mathbf{X}}_t + \tilde{\mathbf{N}}_t, \quad t = 1, 2 \tag{3}$$

where $\tilde{\mathbf{Y}}_t = \log \mathbf{Y}_t$, $\tilde{\mathbf{X}}_t = \log \mathbf{X}_t$, and $\tilde{\mathbf{N}}_t = \log \mathbf{N}_t$. The pdf of the random $\tilde{\mathbf{N}}_t$ is given by [33]

$$p_{\tilde{N}_t}\left(\tilde{N}_t\right) = p_{N_t}\left(e^{\tilde{N}_t}\right) e^{\tilde{N}_t} = \frac{L_t^{L_t}}{\Gamma(L_t)} e^{L_t \tilde{N}_t} e^{-L_t e^{\tilde{N}_t}}. \tag{4}$$

Subtract $\tilde{\mathbf{Y}}_1$ and $\tilde{\mathbf{Y}}_2$, we can obtain the logarithmic DI

$$\tilde{\mathbf{Y}}_D = \tilde{\mathbf{Y}}_1 - \tilde{\mathbf{Y}}_2 = \tilde{\mathbf{X}}_1 - \tilde{\mathbf{X}}_2 + \tilde{\mathbf{N}}_1 - \tilde{\mathbf{N}}_2. \tag{5}$$

To exploit the nonlocal self-similarity, first, a logarithmic DI is divided into a number of overlapped squared patches with size $p_s \times p_s$ and sliding step s_{step}. Then, for each target patch, we select $(N_p - 1)$ most similar patches in the $w_s \times w_s$ search window. Unlike the traditional Euclidean distance used in additive white Gaussian noise condition, some researchers use the following similarity distance for multiplicative speckle noise, which has been proved to be well suited to SAR images

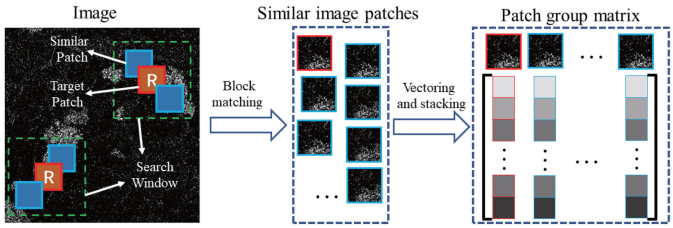

Fig. 2. Illustration of PGM construction.

[23], [34]

$$S_{m,n} = \sum_{k=1}^{p_s^2} \log\left(\frac{\sqrt{I_m(k)}}{\sqrt{I_n(k)}} + \frac{\sqrt{I_n(k)}}{\sqrt{I_m(k)}}\right) \tag{6}$$

where $I_m(k)$ and $I_n(k)$ are the original intensity values of the kth pixel in patches m and n, respectively. The greater the difference between image patches, the bigger $S_{m,n}$ is. Conversely, when the two patches are identical, $S_{m,n}$ reaches the minimum as $S_{n,n} = p_s^2 \log 2$. Inspired by their work, we use the following equation to measure the similarity distance between the patches m and n by substituting $\tilde{I}(k) = \log I(k)$ into (6)

$$\begin{aligned}\tilde{S}_{m,n} &= \sum_{k=1}^{p_s^2} \log\left(\frac{\sqrt{e^{\tilde{I}_m(k)}}}{\sqrt{e^{\tilde{I}_n(k)}}} + \frac{\sqrt{e^{\tilde{I}_n(k)}}}{\sqrt{e^{\tilde{I}_m(k)}}}\right) \\ &= \sum_{k=1}^{p_s^2} \log\left(e^{\tilde{I}_m(k)} + e^{\tilde{I}_n(k)}\right) - \frac{\tilde{I}_m(k) + \tilde{I}_n(k)}{2}\end{aligned} \tag{7}$$

where $\tilde{I}_m(k)$ and $\tilde{I}_n(k)$ are the intensity values of the kth pixel in patches m and n in the logarithmic DI, respectively. After selecting the $(N_p - 1)$ most similar patches, we vectorize and stack them (include the target one) into a patch group matrix (PGM) with the size $p_s^2 \times N_p$. Fig. 2 shows the process of PGM construction.

It is reasonable to assume that the clean PGM, denoted as $\mathbf{\Phi}_i$, should have a low-rank property as all image patches in PGM have a similar underlying structure. Let $\mathbf{R}_i$ stand for the operation matrix that extracting the ith PGM from an image, i.e., $\mathbf{\Phi}_i = \mathbf{R}_i(\tilde{\mathbf{X}}_1 - \tilde{\mathbf{X}}_2)$, then we have the following NLR model for DI:

$$\begin{aligned}&\min \sum_i \mathrm{Rank}\left(\mathbf{\Phi}_i\right) \\ &\text{s.t. } \mathbf{\Phi}_i = \mathbf{R}_i\left(\tilde{\mathbf{X}}_1 - \tilde{\mathbf{X}}_2\right), \tilde{\mathbf{X}}_1 = \tilde{\mathbf{Y}}_1 - \tilde{\mathbf{N}}_1, \tilde{\mathbf{X}}_2 = \tilde{\mathbf{Y}}_2 - \tilde{\mathbf{N}}_2.\end{aligned} \tag{8}$$

The corresponding unconstrained problem is

$$\begin{aligned}&\min D\left(\tilde{\mathbf{X}}_1, \tilde{\mathbf{Y}}_1\right) + D\left(\tilde{\mathbf{X}}_2, \tilde{\mathbf{Y}}_2\right) \\ &\quad + \lambda \sum_i \mathrm{Rank}\left(\mathbf{R}_i\left(\tilde{\mathbf{X}}_1 - \tilde{\mathbf{X}}_2\right)\right)\end{aligned} \tag{9}$$

where $D(\tilde{\mathbf{X}}, \tilde{\mathbf{Y}})$ is the data fidelity term, and λ is a tradeoff parameter. An intuitive requirement is that $D(\tilde{\mathbf{X}}, \tilde{\mathbf{Y}})$ should be proportional to conditional probability. Here, we set $D(\tilde{\mathbf{X}}, \tilde{\mathbf{Y}})$ be the negative logarithm of $p_{\tilde{\mathbf{Y}}|\tilde{\mathbf{X}}}(\tilde{\mathbf{Y}}|\tilde{\mathbf{X}})$. By using (4), we have

$$\begin{aligned}D\left(\tilde{\mathbf{X}}_t, \tilde{\mathbf{Y}}_t\right) &= -\log p_{\tilde{\mathbf{Y}}_t|\tilde{\mathbf{X}}_t}\left(\tilde{\mathbf{Y}}_t \middle| \tilde{\mathbf{X}}_t\right) \\ &= -\log p_{\tilde{\mathbf{N}}_t}\left(\tilde{\mathbf{Y}}_t - \tilde{\mathbf{X}}_t\right) \\ &= c_t + L_t \sum_{s=1}^{M}\left(\tilde{x}_t^s + e^{\tilde{y}_t^s - \tilde{x}_t^s}\right)\end{aligned} \tag{10}$$

where c_t is a constant, $M = I \times J$ is the total number of pixels, and $\tilde{x}_t^s$ and $\tilde{y}_t^s$ are the sth pixel values in $\tilde{\mathbf{X}}_t$ and $\tilde{\mathbf{Y}}_t$, respectively. As the original rank minimization problem is NP-hard, the nuclear norm is usually applied to be the regularization term. To improve the performance, we select the WNN [31], [35] to replace the matrix rank. Substitute (10) and the WNN into (9), and introduce auxiliary variables $\mathbf{z}_i \in \mathbb{R}^{p_s^2 \times N_p}$, we can rewrite the model (9) as

$$\begin{aligned}\left\langle \hat{\mathbf{X}}_1, \hat{\mathbf{X}}_2 \right\rangle = \arg\min_{\tilde{\mathbf{X}}_1, \tilde{\mathbf{X}}_2} &L_1 \sum_{s=1}^{M}\left(\tilde{x}_1^s + e^{\tilde{y}_1^s - \tilde{x}_1^s}\right) \\ &+ L_2 \sum_{s=1}^{M}\left(\tilde{x}_2^s + e^{\tilde{y}_2^s - \tilde{x}_2^s}\right) + \lambda \sum\nolimits_i \left\|\mathbf{z}_i\right\|_{\mathbf{w},*} \\ \text{s.t.} \quad \mathbf{z}_i &= \mathbf{R}_i\left(\tilde{\mathbf{X}}_1 - \tilde{\mathbf{X}}_2\right)\end{aligned} \tag{11}$$

where $\|\mathbf{z}_i\|_{\mathbf{w},*} = \sum_a w_a \sigma_a(\mathbf{z}_i)$ with $\sigma_a(\mathbf{z}_i)$ denoting the ath singular value of $\mathbf{z}_i$, and w_a is the corresponding weight parameter. The augmented Lagrangian function of the objective function (11) is

$$\begin{aligned}&\mathcal{L}\left(\mathbf{z}, \tilde{\mathbf{X}}_1, \tilde{\mathbf{X}}_2, \mathbf{u}\right) \\ &= L_1 \sum_{s=1}^{M}\left(\tilde{x}_1^s + e^{\tilde{y}_1^s - \tilde{x}_1^s}\right) + L_2 \sum_{s=1}^{M}\left(\tilde{x}_2^s + e^{\tilde{y}_2^s - \tilde{x}_2^s}\right) \\ &\quad + \lambda \sum\nolimits_i \left\|\mathbf{z}_i\right\|_{\mathbf{w},*} + \left\langle \mathbf{u}_i, \mathbf{R}_i\left(\tilde{\mathbf{X}}_1 - \tilde{\mathbf{X}}_2\right) - \mathbf{z}_i \right\rangle \\ &\quad + \frac{\rho}{2}\left\|\mathbf{R}_i\left(\tilde{\mathbf{X}}_1 - \tilde{\mathbf{X}}_2\right) - \mathbf{z}_i\right\|_F^2\end{aligned} \tag{12}$$

where $\langle \cdot, \cdot \rangle$ denotes the inner product, $\mathbf{u}_i \in \mathbb{R}^{p_s^2 \times N_p}$ is the Lagrangian multiplier, and $\rho > 0$ is the penalty parameter, which is selected to balance the regularization and data fidelity. Then, we can use the ADM to solve the minimization of (12) by separating it into $\mathbf{z}$-subproblem and $\tilde{\mathbf{X}}$-subproblem.

First, suppose that we have $(\mathbf{z}^k, \tilde{\mathbf{X}}_1^k, \tilde{\mathbf{X}}_2^k, \mathbf{u}^k)$ at the kth iteration, then the minimization of (12) with respect to $\mathbf{z}$ can be formulated as

$$\begin{aligned}\mathbf{z}^{k+1} = \arg\min_{\mathbf{z}} &\sum_i \left\|\mathbf{z}_i\right\|_{\mathbf{w},*} \\ &+ \frac{\rho}{2}\left\|\mathbf{R}_i\left(\tilde{\mathbf{X}}_1^k - \tilde{\mathbf{X}}_2^k\right) - \mathbf{z} + \frac{\mathbf{u}_i^k}{\rho}\right\|_F^2.\end{aligned} \tag{13}$$

Then, we can update $\mathbf{z}^{k+1}$ as

$$\mathbf{z}_i^{k+1} = \mathbf{U}\mathrm{soft}\left(\mathbf{\Sigma}, \frac{1}{\rho}\mathrm{diag}\left(\mathbf{w}\right)\right)\mathbf{V}^T \tag{14}$$

where $\mathbf{U}\mathbf{\Sigma}\mathbf{V}^T$ is the singular value decomposition (SVD) of $[\mathbf{R}_i(\tilde{\mathbf{X}}_1^k - \tilde{\mathbf{X}}_2^k) + \frac{\mathbf{u}_i^k}{\rho}]$ and the soft threshold here is defined as $\text{soft}(x,t) = \max\{x-t, 0\}$. According to [31], the ath element of $\mathbf{w}$ is set to be inversely proportional to $\sigma_a(\mathbf{R}_i(\tilde{\mathbf{X}}_1^k - \tilde{\mathbf{X}}_2^k) + \frac{\mathbf{u}_i^k}{\rho})$. Here, we set $w_a = \frac{\sqrt{N_p}}{\Sigma_a + \varepsilon}$ with $\varepsilon = 10^{-16}$ to avoid dividing by zero.

With the fixed $(\mathbf{z}^{k+1}, \tilde{\mathbf{X}}_2^k, \mathbf{u}^k)$, the minimization of (12) with respect to $\tilde{\mathbf{X}}_1$ can be formulated as

$$\begin{aligned}\tilde{\mathbf{X}}_1^{k+1} = \ & \arg\min_{\tilde{\mathbf{X}}_1} L_1 \sum_{s=1}^{M} \left(\tilde{x}_1^s + e^{\tilde{y}_1^s - \tilde{x}_1^s}\right) \\ & + \lambda \sum_i \frac{\rho}{2} \left\| \mathbf{R}_i \left(\tilde{\mathbf{X}}_1 - \tilde{\mathbf{X}}_2^k\right) - \mathbf{z}^{k+1} + \frac{\mathbf{u}_i^k}{\rho} \right\|_F^2 \end{aligned} \quad (15)$$

which is a convex problem. Taking derivation on the objective function of (15) with respect to $\tilde{\mathbf{X}}_1$ and forcing the result to zero, we can obtain

$$\begin{aligned} & L_1 - L_1 e^{\tilde{\mathbf{Y}}_1 - \tilde{\mathbf{X}}_1} \\ & \quad = -\lambda\rho \sum_i \mathbf{R}_i^T \left(\mathbf{R}_i \left(\tilde{\mathbf{X}}_1 - \tilde{\mathbf{X}}_2^k\right) - \mathbf{z}^{k+1} + \frac{\mathbf{u}_i^k}{\rho} \right). \end{aligned} \quad (16)$$

It is not easy to obtain the closed-form solution even with the Lambert W function. To avoid this difficult computational process, we use the linearize inexact approximation technique and modify $\frac{1}{2}\|\mathbf{R}_i(\tilde{\mathbf{X}}_1 - \tilde{\mathbf{X}}_2^k) - \mathbf{z}^{k+1} + \frac{\mathbf{u}_i^k}{\rho}\|_F^2$ as

$$\begin{aligned} & \frac{1}{2} \left\| \mathbf{R}_i \left(\tilde{\mathbf{X}}_1 - \tilde{\mathbf{X}}_2^k\right) - \mathbf{z}^{k+1} + \frac{\mathbf{u}_i^k}{\rho} \right\|_F^2 \\ & \approx \frac{1}{2} \left\| \mathbf{R}_i \left(\tilde{\mathbf{X}}_1^k - \tilde{\mathbf{X}}_2^k\right) - \mathbf{z}^{k+1} + \frac{\mathbf{u}_i^k}{\rho} \right\|_F^2 \\ & \quad + \left\langle \mathbf{R}_i^T \left(\mathbf{R}_i \left(\tilde{\mathbf{X}}_1^k - \tilde{\mathbf{X}}_2^k\right) - \mathbf{z}^{k+1} + \frac{\mathbf{u}_i^k}{\rho} \right), \tilde{\mathbf{X}}_1 - \tilde{\mathbf{X}}_1^k \right\rangle \\ & \quad + \frac{1}{2\tau_i} \left\| \tilde{\mathbf{X}}_1 - \tilde{\mathbf{X}}_1^k \right\|_F^2 \end{aligned} \quad (17)$$

where $\tau_i > 0$ is the step size. Substitute (17) into (15), and rewrite the derivation equation as

$$\begin{aligned} L_1 - L_1 e^{\tilde{\mathbf{Y}}_1 - \tilde{\mathbf{X}}_1} = \ & -\lambda\rho \sum_i \mathbf{R}_i^T \left(\mathbf{R}_i \left(\tilde{\mathbf{X}}_1^k - \tilde{\mathbf{X}}_2^k\right) \right. \\ & \left. - \mathbf{z}^{k+1} + \frac{\mathbf{u}_i^k}{\rho} \right) + \frac{\tilde{\mathbf{X}}_1 - \tilde{\mathbf{X}}_1^k}{\tau_i}. \end{aligned} \quad (18)$$

Although its closed-form solution can be obtained by using the Lambert W function, here we apply the Newton method as it can yield a fast and accurate solution by a few iterations (in general, five iterations in our problem are enough to obtain an approximate exact solution). The update formula for Newton method is given by (19), shown at the bottom of this page. In (19), the point division sign $./$ is defined as the elementwise division $(\mathbf{A}./\mathbf{B})_{ij} = (a_{ij}/b_{ij})$

Similarly, with the fixed $(\mathbf{z}^{k+1}, \tilde{\mathbf{X}}_1^{k+1}, \mathbf{u}^k)$, the minimization of (12) with respect to $\tilde{\mathbf{X}}_2$ can be formulated as

$$\begin{aligned} \tilde{\mathbf{X}}_2^{k+1} = \ & \arg\min_{\tilde{\mathbf{X}}_2} L_2 \sum_{s=1}^{M} \left(\tilde{x}_2^s + e^{\tilde{y}_2^s - \tilde{x}_2^s}\right) \\ & + \lambda \sum_i \frac{\rho}{2} \left\| \mathbf{R}_i \left(\tilde{\mathbf{X}}_2 - \tilde{\mathbf{X}}_1^{k+1}\right) + \mathbf{z}^{k+1} - \frac{\mathbf{u}_i^k}{\rho} \right\|_F^2. \end{aligned} \quad (20)$$

Taking the same processing steps as $\tilde{\mathbf{X}}_1$, we can update $\tilde{\mathbf{X}}_2$ by using the linearize inexact approximation and Newton iteration as (21) shown at the bottom of this page.

Finally, we update the Lagrangian multipliers and penalty parameter ρ as

$$\mathbf{u}_i^{k+1} = \mathbf{u}_i^k + \rho \left(\mathbf{R}_i \left(\tilde{\mathbf{X}}_1^{k+1} - \tilde{\mathbf{X}}_2^{k+1}\right) - \mathbf{z}_i^{k+1} \right) \quad (22)$$

$$\rho \leftarrow \mu \times \rho \quad (23)$$

where $\mu > 1$.

It should be noticed that the NLR model for DI is not equal to the denoising operation on the log-ratio image $\tilde{\mathbf{Y}}_D$, which constructs the NLR model as

$$\begin{aligned} \min_{\tilde{\mathbf{X}}_1 - \tilde{\mathbf{X}}_2} \ & D\left(\tilde{\mathbf{X}}_1 - \tilde{\mathbf{X}}_2 \middle| \tilde{\mathbf{Y}}_1 - \tilde{\mathbf{Y}}_2\right) \\ & + \lambda \sum_i \text{Rank}\left(\mathbf{R}_i \left(\tilde{\mathbf{X}}_1 - \tilde{\mathbf{X}}_2\right)\right). \end{aligned} \quad (24)$$

Although this model is easier to be solved than (9), it loses data information in the process of subtraction as can be seen by comparing it with model (9), where the data fidelity terms $D(\tilde{\mathbf{X}}_1, \tilde{\mathbf{Y}}_1)$ and $D(\tilde{\mathbf{X}}_2, \tilde{\mathbf{Y}}_2)$ are both used. This means that the proposed NLR model makes fuller use of the information of the original images, and, thus, leads to a better performance.

Our algorithm, named NLR-driven ADMMs for DI generation (NLR-ADMM for short), is summarized in Table I. Briefly, the ADMM algorithm for NLR model of DI (12) makes full use of the separable structure of the objective function and iteratively solve the $\mathbf{z}$-subproblem and $\tilde{\mathbf{X}}$-subproblem. One subproblem can be solved by the weighted singular value threshold method, and the other can be solved by the efficient inexact linearization technique and Newton method. Since calculating

$$\tilde{\mathbf{X}}_1 \leftarrow \tilde{\mathbf{X}}_1 - \left(L_1 - L_1 e^{\tilde{\mathbf{Y}}_1 - \tilde{\mathbf{X}}_1} + \lambda\rho \sum_i \mathbf{R}_i^T \left(\mathbf{R}_i \left(\tilde{\mathbf{X}}_1^k - \tilde{\mathbf{X}}_2^k\right) - \mathbf{z}^{k+1} + \frac{\mathbf{u}_i^k}{\rho} \right) + \frac{\tilde{\mathbf{X}}_1 - \tilde{\mathbf{X}}_1^k}{\tau_i} \right) . \Big/ \left(L_1 e^{\tilde{\mathbf{Y}}_1 - \tilde{\mathbf{X}}_1} + \lambda\rho \sum_i \frac{1}{\tau_i} \right) \quad (19)$$

$$\tilde{\mathbf{X}}_2 \leftarrow \tilde{\mathbf{X}}_2 - \left(L_2 - L_2 e^{\tilde{\mathbf{Y}}_2 - \tilde{\mathbf{X}}_2} + \lambda\rho \sum_i \mathbf{R}_i^T \left(\mathbf{R}_i \left(\tilde{\mathbf{X}}_2^k - \tilde{\mathbf{X}}_1^k\right) + \mathbf{z}^{k+1} - \frac{\mathbf{u}_i^k}{\rho} \right) + \frac{\tilde{\mathbf{X}}_2 - \tilde{\mathbf{X}}_2^k}{\tau_i} \right) . \Big/ \left(L_2 e^{\tilde{\mathbf{Y}}_2 - \tilde{\mathbf{X}}_2} + \lambda\rho \sum_i \frac{1}{\tau_i} \right) \quad (21)$$

TABLE I
IMPLEMENTATION STEPS OF NLR-ADMM FOR DI GENERATION

Algorithm 1. NLR-ADMM for DI generation

Initialization:

Given $\mathbf{Y}_1$, $\mathbf{Y}_1$, L_1, L_2. Select ρ, μ, λ, $\boldsymbol{\tau}$, N_{iter}, and ξ_0.

Initialize $\tilde{\mathbf{X}}_1^0 = \tilde{\mathbf{Y}}_1$, $\tilde{\mathbf{X}}_2^0 = \tilde{\mathbf{Y}}_2$.

Main iteration loop:

for $k = 1, 2, \cdots, N_{iter}$ do

if $\mathrm{mod}(k, \mathrm{I}_R) == 0$

Calculate the similarity metric for each target patch and establish $\{\mathbf{R}_i\}$.

End if

$\mathbf{z}$-updating: compute $\mathbf{z}^{k+1}$ according to (14).

$\tilde{\mathbf{X}}_1$-updating: compute $\tilde{\mathbf{X}}_1^{k+1}$ according to (19) with a few Newton iterations.

$\tilde{\mathbf{X}}_2$-updating: compute $\tilde{\mathbf{X}}_2^{k+1}$ according to (21) with a few Newton iterations.

$\mathbf{u}_i$-updating: compute $\mathbf{u}_i^{k+1}$ according to (22).

ρ-updating as $\rho \leftarrow \mu \times \rho$.

Exit criterion: $\xi^{k+1} = \min\left\{ \left\|\tilde{\mathbf{X}}_1^{k+1} - \tilde{\mathbf{X}}_1^{k}\right\|_2 / \left\|\tilde{\mathbf{X}}_1^{k}\right\|_2, \left\|\tilde{\mathbf{X}}_2^{k+1} - \tilde{\mathbf{X}}_2^{k}\right\|_2 / \left\|\tilde{\mathbf{X}}_2^{k}\right\|_2 \right\}$

if $\xi^{k+1} < \xi_0$ then

exit

End if

End for

Return $\tilde{\mathbf{X}}_D = \left|\tilde{\mathbf{X}}_1^{k+1} - \tilde{\mathbf{X}}_2^{k+1}\right|$

the similarity metric for each patch and constructing the patch group extracting matrix $\{\mathbf{R}_i\}$ are time-consuming, moreover, it is not updated much in two adjacent iterations, this step is only carried out once every I_R iterations to reduce computational complexity.

As shown in Table I, the N_{iter} is the max number of reconstruction iterations, ξ^{k+1} is the minimum ℓ_2-distance between two iterative results. The exit criterion $\xi^{k+1} < \xi_0$ means that there is no longer any appreciate changes in the iteration and NLR-ADMM runs into convergence. Meanwhile, the ENL parameters L_1 and L_2 can be obtained according to prior knowledge, or can be estimated from the homogeneous region of $\tilde{\mathbf{Y}}_1$ and $\tilde{\mathbf{Y}}_2$ as [36], respectively

$$\mathrm{ENL} = S_C \left(\frac{\mu_{HR}}{\sigma_{HR}}\right)^2, \qquad S_C = \begin{cases} 1, & \text{intensity image} \\ 4/\pi - 1, & \text{amplitude image} \end{cases} \tag{25}$$

where μ_{HR} is the mean value of the selected homogeneous region and σ_{HR}^2 is the corresponding variance.

B. PCA Feature Extraction

Although there are many methods to extract the features from the DI, such as Gabor wavelets [26], compressed projection [15], here we use the PCA to extract the eigen-vectors as in [25] for its simplicity and efficiency. PCA uses a subset of the principle components to represent the original signal so that most of the energy is preserved, while the energy of noise will evenly spread over the whole dataset. Compared with the direct usage of PCA on the log-ratio DI, the NLR model based DI can enhance the low-rank property of the DI and reduce the speckle noise, which can help the PCA to extract more effective features and make up for the deficiency of PCA in despeckling, as PCA is more suitable for the data which follows Gaussian distribution. Thus, combining NLR-ADMM for DI with PCA feature extracting can improve the CD performance.

First, the $h \times h$ ($h \geq 2$) nonoverlapping image blocks are partitioned from the DI $\tilde{\mathbf{X}}_D$ obtained by using the above NLR-ADMM. For each block, we vectorize it and arrange them into a matrix. Second, by calculating the mean vector and the covariance matrix, the eigenvector space is obtained by applying the PCA. Third, by projecting the overlapping $h \times h$ data block around each pixel onto eigenvector space, the corresponding feature vector $\mathbf{q}$ with s dimension can be extracted, where $1 \leq s \leq h^2$. Then, we can obtain the feature matrix $\mathbf{Q} = [\mathbf{q}_1, \ldots, \mathbf{q}_{I \times J}]^T$ over the entire DI with the size $(I \times J) \times s$ to represent the $I \times J$ pixels in the DI $\tilde{\mathbf{X}}_D$.

C. Modified Two-Level Clustering

Once the features of DI have been extracted, clustering methods are often employed to obtain the classification result, such as the K-means clustering, FCM clustering, and their variants. Due to the overlap of the changed and unchanged classes, the commonly used one-step clustering algorithm sometimes fails to make a reliable decision. To addresses this challenge, Li *et al.* have proposed a two-level clustering method [26], where they have designed a cascade structure with two simple clustering algorithms to implement a coarse-to-fine discrimination. Especially, in the first level clustering, FCM is employed on the feature matrix $\mathbf{Q}$ to partition $\tilde{\mathbf{X}}_D$ into three clusters. By using the FCM, we can obtain the matrix $\boldsymbol{\mu} = [\mu_{mn}]_{3 \times IJ}$ with μ_{mn} representing the membership grade of nth pixel in cluster m, and centroid matrix $\boldsymbol{\nu} = [\nu_1, \nu_2, \nu_3]$ with $\nu_m \in \mathbb{R}^s$ representing the centroid of cluster m. First, we divide each pixel into an initial class Ω_m by the maximum membership principle from $\boldsymbol{\mu}$, and, then, calculate the mean value of $\tilde{\mathbf{X}}_D$ in cluster Ω_m as $M_{\Omega_m} = (1/|\Omega_m|) \sum_{n \in \Omega_m} \tilde{x}_D^n$. Then, we can determine, which cluster Ω_m corresponds to the changed, unchanged, and indeterminate class by comparing the values of M_{Ω_m}, which are

defined as w_c, w_u, and w_i, respectively

$$\Omega_m = \begin{cases} w_c, & m = \arg\max_{m=1,2,3} M_{\Omega_m} \\ w_u, & m = \arg\min_{m=1,2,3} M_{\Omega_m} \\ w_i, & \text{otherwise.} \end{cases} \tag{26}$$

In the second-level clustering, the centroids of w_c and w_u are recalculated by

$$\nu_{w_c} = \frac{\sum_{n\in w_c} \mu_{mn}^2 \mathbf{q}_n}{\sum_{n\in w_c} \mu_{mn}^2}, \quad m \to \text{label}\,(w_c) \tag{27}$$

$$\nu_{w_u} = \frac{\sum_{n\in w_u} \mu_{mn}^2 \mathbf{q}_n}{\sum_{n\in w_u} \mu_{mn}^2}, \quad m \to \text{label}\,(w_u)\,. \tag{28}$$

Unlike in [26], where the nearest neighbor rule is simply employed to separate w_i into two class as

$$n \in \begin{cases} w_c, & \left\|\mathbf{q}_n - \nu_{w_c}\right\|_2 \le \left\|\mathbf{q}_n - \nu_{w_u}\right\| \\ w_u, & \left\|\mathbf{q}_n - \nu_{w_c}\right\|_2 > \left\|\mathbf{q}_n - \nu_{w_u}\right\| \end{cases}, \; n \in w_i. \tag{29}$$

Here, we separate the intermediate class by using the neighbor information with Gaussian weighted distance. As the intermediate class w_i is between the highly pure changed class w_c and unchanged class w_u, thus most of errors will be concentrated in this reclassification process. Considering that each changed or unchanged pixel is not isolated, and by using this homogeneity of the changed and unchanged portions, the Gaussian weighted distance classification rule is proposed. After centroids of w_c and w_u are obtained by (27) and (28), we calculate two distance maps $\mathbf{d}^c = [d_{i,j}^c]_{I\times J}$ and $\mathbf{d}^u = [d_{i,j}^u]_{I\times J}$ to these two centroids for each pixel $\tilde{x}_D(i,j)$ in $\tilde{\mathbf{X}}_D$ as

$$d_{i,j}^c = \left\|\mathbf{q}_{i,j} - \nu_{w_c}\right\|_2, \quad d_{i,j}^u = \left\|\mathbf{q}_{i,j} - \nu_{w_u}\right\|_2 \tag{30}$$

where $\mathbf{q}_{i,j}$ is the feature vector of pixel $\tilde{x}_D(i,j)$, i.e., $\mathbf{q}_{i,j} = \mathbf{q}_{(i-1)\times I+j}$ in feature matrix $\mathbf{Q}$. Then, for each pixel $\tilde{x}_D(i,j)$ in w_i, we calculate its weighted distances to the centroids of w_c and w_u as

$$\tilde{d}_{i,j}^c = \sum_{h=-1}^{1}\sum_{t=-1}^{1} g_{h,t} d_{i+h,j+t}^c$$

$$\tilde{d}_{i,j}^u = \sum_{h=-1}^{1}\sum_{t=-1}^{1} g_{h,t} d_{i+h,j+t}^u \tag{31}$$

where $g_{h,t}$ is the element of the rotationally symmetric Gaussian low-pass filter $\mathbf{G}$ of size 3×3 with standard deviation 0.5 as follows:

$$\mathbf{G} = \begin{bmatrix} g_{-1,-1} & g_{-1,0} & g_{-1,1} \\ g_{0,-1} & g_{0,0} & g_{0,1} \\ g_{1,-1} & g_{1,0} & g_{1,1} \end{bmatrix} = \begin{bmatrix} 0.0113 & 0.0838 & 0.0113 \\ 0.0838 & 0.6193 & 0.0838 \\ 0.0113 & 0.0838 & 0.0113 \end{bmatrix}. \tag{32}$$

Then, we can divide w_i into changed or unchanged class according to nearest distance criterion as

$$n \in \begin{cases} w_c, & \tilde{d}_{i,j}^c \le \tilde{d}_{i,j}^u \\ w_u, & \tilde{d}_{i,j}^c > \tilde{d}_{i,j}^u \end{cases}, \text{ with } n \in w_i,\; n = (i-1)\times I + j. \tag{33}$$

As a result, we can obtain the final binary change map $\mathbf{CM} = \{cm(i,j) | 1 \le i \le I, 1 \le j \le I\}$, in which $cm(i,j) = 1$ indicates that the changed location with $n \in w_c$, whereas $cm(i,j) = 0$ involving unchanged location with $n \in w_u$, with $n = (i-1)\times I + j$.

III. Experimental Analysis

In this section, simulations are performed to demonstrate the proposed conclusions and evaluate the performance of the proposed NLR-PCATLC based CD method. We apply six methods in comparison: PCA with k-means clustering (PCA-KM) [25], modified Markov random field with FCMs (MRFFCM) [30], neighborhood-based ratio and extreme learning machine method (NR-ELM) [37], Gabor feature with two-level clustering (GaborTLC) [26], PCANet [38], and convolutional-wavelet neural network (CWNN) [39].

In order to evaluate the performance of different methods, we use some quantitative parameters to evaluate the final map: false negatives (FN), false positives (FP), the overall error (OE), the percentage correct classification (PCC) and the Kappa coefficient (Kappa). All experiments are performed in MATLAB 2015b running on personal ASUS laptop with Intel Core i7-8550 U CPU, 8 GB of RAM, and 64 bit Windows 10 operating system.

A. Effectiveness of the DI Generation and Clustering Process

In the first experiment, we test the proposed method on the Carabas dataset to verify the effectiveness of the NLR-ADMM and the modified two-level clustering, respectively. Fig. 3 shows the Carabas II VHF dataset, which contains vehicles concealed under foliage obtained from a Sabreliner aircraft with a resolution of 3 m in northern Sweden 2002. From Fig. 3(c), we can find that there are few but strong changes with relatively small area. Fig. 3(d) and (e) show the DIs generated by log-ratio operation and NLR-ADMM, respectively. Fig. 3(f) and (g) shows the CD results by using the PCA-KM with log-ratio based DI of Fig. 3(d) and NLR-ADMM based DI of Fig. 3(e), respectively. By comparing these pictures separately, we can find that the NLR model can generate a better DI than the traditional log-ratio operator, especially in the feature extraction by PCA operation. This is because that the NLR can help the PCA to extract more effective features and make up for the shortcomings of PCA under non-Gaussian distribution, as the NLR model can enhance the low-rank property and reduce the speckle noise. Fig. 3(h) and (i) shows the CD results by using the original two-level clustering in [26] and the Gaussian weighted two-level clustering after the PCA extracting operation on the NLR-ADMM obtained DI of Fig. 3(e), respectively. As pointed in Section II, the modified two-level clustering can use the neighbor information of the intermediate class pixels, then it can reduce the number of isolated points, which may be caused by speckle noise. As can be

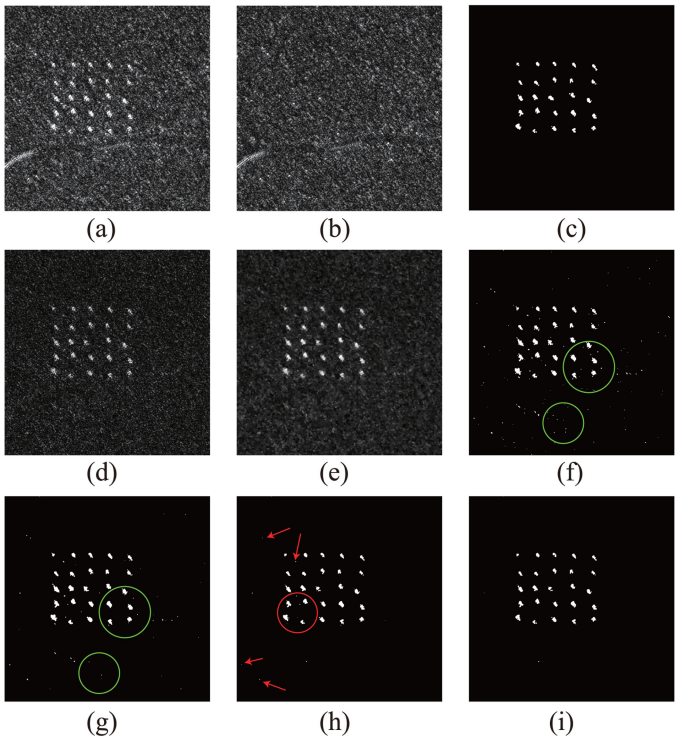

Fig. 3. Test on Carabas dataset: (a) image acquired in time 1; (b) image acquired in time 2; (c) ground truth image; (d) log-ratio generated DI; (e) NLR-ADMM generated DI; (f) PCA-KM with log-ratio based DI, where FN = 77, FP = 798 and Kappa = 0.8171; (g) PCA-KM with NLR-ADMM based DI, where FN = 69, FP = 605 and Kappa = 0.8535; (h) NLR-PCATLC without using the modified Gaussian weighted two-level clustering, where FN = 147, FP = 162 and Kappa = 0.9244; and (i) proposed NLR-PCATLC result, where FN=170, FP = 15 and Kappa = 0.9528.

seen from Fig. 3(h) and (i), the isolated error classification points are well suppressed by using the homogeneity of the changed and unchanged classes, for example, the points marked by the red arrow and the red circle in Fig. 3(h).

B. Test on Other Datasets

Here, we test the proposed NLP-PCATLC with other comparing methods on seven datasets, which include four flood mapping datasets, one farmland change dataset, and two urban building change datasets.

1) Description of the Experimental Data: The first dataset of SAR images is from Bern, Switzerland, in April and May 1999 acquired by ERS-2 SAR sensor with the size 301×301 pixels. Fig. 4(a) and (b) show the two multitemporal SAR images, respectively. Fig. 4(c) shows the ground truth of the CD map, which represents that River Aare inundated parts of Bern, Thun and the whole airport in Bern. The second dataset is from Ottawa, Canada, in May and August 1997, acquired by Radarsat-1 SAR sensor with the size of 290×350 pixels, as shown in Fig. 5(a) and (b), respectively. Fig. 5(c) shows the ground truth of the CD map, which represents a rise in the surface of lakes on the rainy season. The third dataset is from San Francisco, in August 2003 and May 2004, acquired by ERS-2 SAR sensor with the size 256×256 pixels, as shown

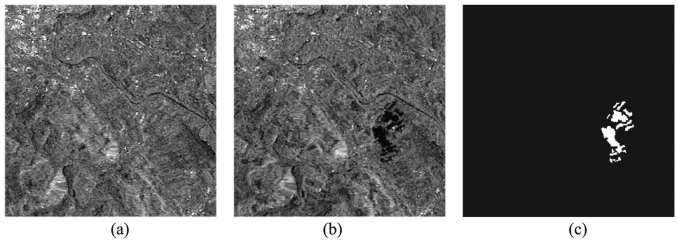

Fig. 4. Bern dataset: (a) image acquired in April 1999; (b) image acquired in May 1999; and (c) ground truth image.

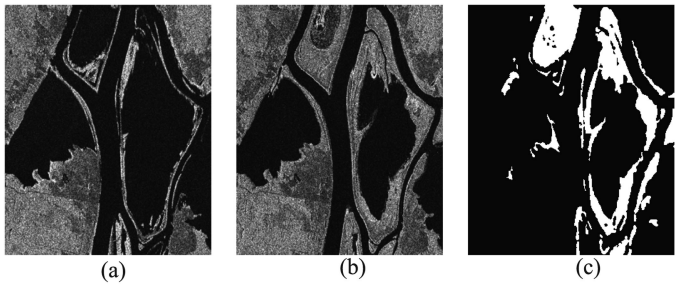

Fig. 5. Ottawa dataset: (a) image acquired in May 1997; (b) image acquired in August 1997; and (c) ground truth image.

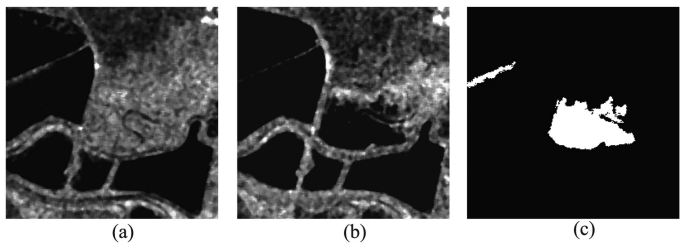

Fig. 6. San Francisco dataset: (a) image acquired in August 2003; (b) image acquired in May 2004; and (c) ground truth image.

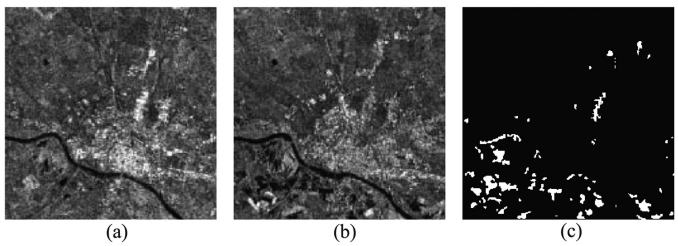

Fig. 7. Italy dataset: (a) image acquired in October 20, 2010; (b) image acquired in October 28, 2010; and (c) ground truth image.

in Fig. 6(a) and (b), respectively. Fig. 6(c) shows the reference image generated by integrating prior information with photograph interpretation. The fourth dataset is from Italy, in October 20 and 28, 2010, acquired by ERS-2 SAR sensor with VV polarization and 256×256 pixels, as shown in Fig. 7(a) and (b). Fig. 7(c) shows the reference image, which represents the changes in the flood event. The fifth dataset is from Yellow River Estuary, China, in June 2008 and June 2009, acquired by Radarsat-2 SAR sensor with the size 257×289 pixels, as shown in Fig. 8(a) and 8(b). Fig. 8(c) shows the reference

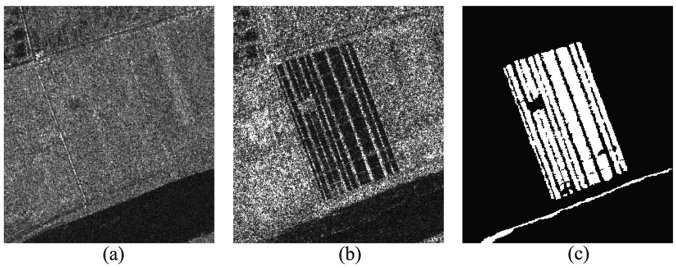

Fig. 8. Yellow River dataset: (a) image acquired in June 2008; (b) image acquired in June 2009; and (c) ground truth image.

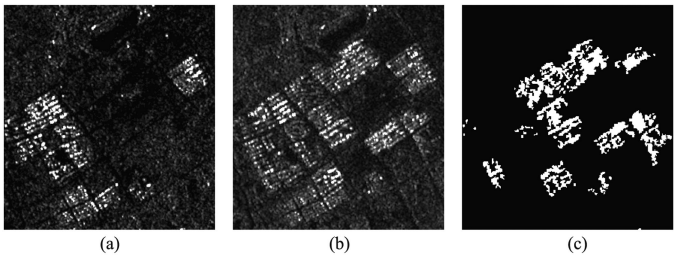

Fig. 9. Yichun dataset: (a) image acquired in August 22, 2017; (b) image acquired in August 24, 2019; and (c) ground truth image.

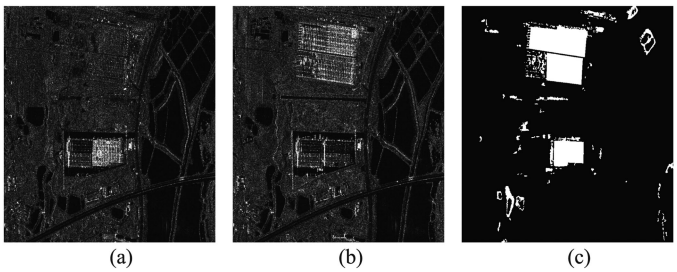

Fig. 10. Wuhan dataset: (a) image acquired in October 14, 2015; (b) image acquired in February 1, 2016; and (c) the ground truth image.

image, which is created by integrating prior information with photo interpretation based on the input images in Fig. 8(a) and (b). The sixth dataset is from the Yichun, China, in 22 August 2017 and 24 August 2019 by Sentinel-1 SAR sensor with VH polarization and 299×282 pixels, as shown in Fig. 9(a) and (b). Fig. 9(c) shows the reference image, which represents the new buildings. The last dataset is from Wuhan, China, in 14 October 2015 and 1 February 2016 by Terra SAR sensor with HH polarization and 870×779 pixels, as shown in Fig. 10(a) and (b). Fig. 10(c) shows the reference image, which represents the new and demolished factories, some changes in waters and other changes like vehicle targets. It should be noted that we adopt two different strategies to label the ground truth maps of the building changes for Yichun dataset and Wuhan dataset. In Fig. 9(c), we label the ground truth mainly based on SAR scattered images, so it has some structures reflecting SAR imaging characteristics. However, we label Fig. 10(c) mainly based on the corresponding optical images, so it can visually reflect the changes of the building area. These two different labeling strategies can fully reflect the performance of all comparison methods in terms of visual effect and parameter evaluation indexes.

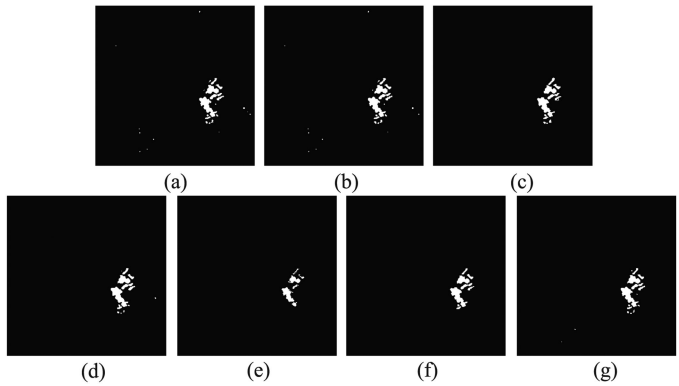

Fig. 11. Final CD maps of Bern dataset generated by: (a) PCA-KM; (b) MRFFCM; (c) NR-ELM; (d) GaborTLC; (e) PCANet; (f) CWNN; and (g) proposed NLR-PCATLC.

TABLE II
QUANTITATIVE MEASURES ON THE BERN DATASET

Methods	FN	FP	OE	PCC(%)	Kappa
PCA-KM	**145**	158	303	99.67	0.8679
MRFFCM	**141**	165	306	99.66	0.8672
NR-ELM	185	118	303	99.67	0.8632
GaborTLC	158	122	**280**	**99.69**	**0.8753**
PCANet	523	**10**	533	99.41	0.7007
CWNN	230	**85**	315	99.65	0.8528
NLR-PCATLC	167	99	**266**	**99.71**	**0.8799**

2) Parameter Setting: Results of PCA-KM, MRFFCM, NR-ELM, GaborTLC, PCANet, and CWNN (http://summitgao.github.io) are implemented by using the authors' public available codes. Therefore, some parameters we used in these methods are the recommended parameters provided in their source codes. Especially, in MRFFCM, the number of subintervals is set to 30 as mentioned in [30]. In GaborTLC, we implement the Gabor wavelet transform with $U = 8, V = 5, k_{\max} = 2\pi$, and $f = \sqrt{2}$, and leave σ to be tuned from 2π to 3π with ten equally spaced. In PCANet, the size of the neighborhood is set as 5×5, while in NR-ELM, the neighborhood size of the NR operator and the feature extraction are set to be 3 and 5 as recommended, respectively. In PCA-KM and NLR-PCATLC, the image blocks size and PCA feature vector size are set to be $h = 5$ and $s = 5$ for San Francisco and Yellow River datasets, and $h = 3$ and $s = 3$ other datasets, respectively. The other parameters for NLR-PCATLC are set as $N_{\text{iter}} = 40$, $\mathrm{I}_R = 4$, $\xi_0 = 10^{-5}$, $p_s = 5$, $w_s = 25$, $s_{\text{step}} = 3$, and $N_p = 10$ in the NLR-ADMM to generate the DI for all these seven datasets.

3) Result Analysis: We first test these methods on the Bern dataset. Fig. 11 shows the final maps of PCA-KM, MRFFCM, NR-ELM, GaborTLC, PCANet, CWNN, and the proposed NLR-PCATLC, and Table II lists the values of the evaluation criteria with the optimal two values written in bold for each criterion. As shown in Fig. 11, the CD maps generated by NLR-PCATLC has little speckles, and the small changes isolated from the main changed area are also well detected. PCA-KM, MRFFCM, and GaborTLC work well on the CD, while they fail on the antispeckle noise and bring more false alarm. The PCANet has the minimum FP, but it is overly smoothing, which

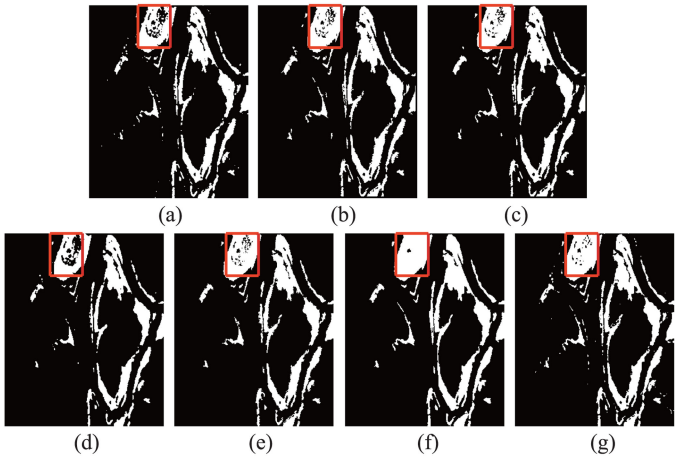

Fig. 12. Final CD maps of Ottawa dataset generated by: (a) PCA-KM; (b) MRFFCM; (c) NR-ELM; (d) GaborTLC; (e) PCANet; (f) CWNN; and (g) proposed NLR-PCATLC.

TABLE III
QUANTITATIVE MEASURES ON THE OTTAWA DATASET

Methods	FN	FP	OE	PCC(%)	Kappa
PCA-KM	1901	582	2483	97.55	0.9049
MRFFCM	1356	815	2171	97.86	0.9185
NR-ELM	1267	**514**	1781	98.25	0.9328
GaborTLC	2532	**213**	2745	97.30	0.8921
PCANet	1158	619	1777	98.25	0.9333
CWNN	**434**	1291	**1725**	**98.30**	**0.9375**
NLR-PCATLC	**608**	903	**1511**	**98.51**	**0.9445**

makes many of the changed pixel undetected. Even though the FN and FP of NLR-PCATLC and GaborTLC are not the least, they could provide an acceptable detection results, which work well on both the denoising and edge preserving, thus they bring a higher Kappa coefficient, as shown in Table II.

The result of the second experiment on the Ottawa dataset are shown in Fig. 12 and listed in Table III, respectively. As shown in Fig. 12(g), the CD map produced by NLR-PCATLC is closer to the reference image and preserves more details than other methods, thus leads to the least FN as 608, which is much less than GaborTLC, PCA-KM, and other methods except the CWNN. This mainly due to that NLR model can well preserve the image details and edges, as pointed out by the red rectangle box in Fig. 12. Meanwhile, because the speckle noise level in the two original multitemporal images is relatively low as can be seen from Fig. 5(a) and (b), the denoising effect of NLR-PCATLC is not so obvious. However, NLR-PCATLC is still optimal in terms of both OE, PCC, and Kappa coefficient, which demonstrates the effectiveness of the proposed method again.

The CD maps generated by different methods on the San Francisco dataset are shown in Fig. 13 with their values of evaluation criteria listed in Table IV. There are many isolated white spots in GaborTLC, PCA-KM, and MRFFCM, which bring more false alarm and cause the high value of FP as 763, 701, and 523 in Table IV. The PCANet have the least FP, but it fails on the detection of some details and leads to highest FN. Comparing to other methods, the OE, PCC, and Kappa coefficients of NLR-PCATLC and CWNN are superior to those of others, which indicates that they will perform better when a more accurate result is required.

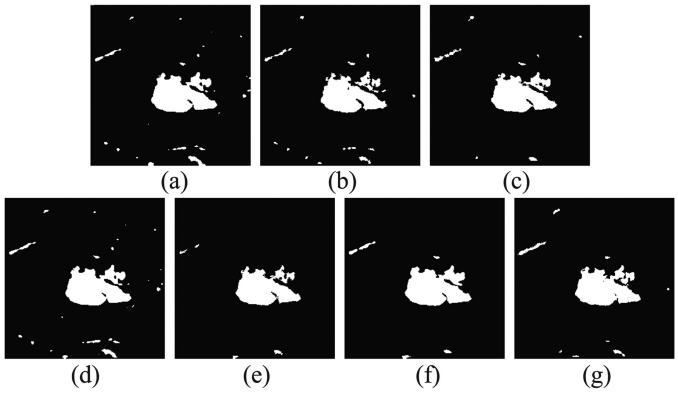

Fig. 13. Final CD maps of San Francisco dataset generated by: (a) PCA-KM; (b) MRFFCM; (c) NR-ELM; (d) GaborTLC; (e) PCANet; (f) CWNN; and (g) proposed NLR-PCATLC.

TABLE IV
QUANTITATIVE MEASURES ON THE SAN FRANCISCO DATASET

Methods	FN	FP	OE	PCC(%)	Kappa
PCA-KM	378	701	1079	98.35	0.8798
MRFFCM	568	523	1091	98.34	0.8740
NR-ELM	471	**358**	829	98.74	0.9036
GaborTLC	**324**	763	1087	98.34	0.8802
PCANet	642	**142**	784	98.80	0.9052
CWNN	**295**	437	**732**	**98.88**	**0.9170**
NLR-PCATLC	375	378	**753**	**98.85**	**0.9135**

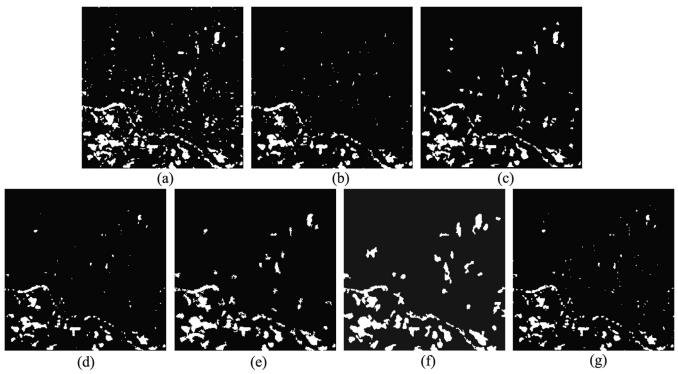

Fig. 14. Final CD maps of Italy dataset generated by: (a) PCA-KM; (b) MRFFCM; (c) NR-ELM; (d) GaborTLC; (e) PCANet; (f) CWNN; and (g) proposed NLR-PCATLC.

Fig. 14 shows the CD maps of different methods on the Italy dataset, and Table V lists the corresponding values of evaluation criteria. From these, we can find that the GaborTLC and NLR-PCATLC can provide better results when comparing with other methods. By comparing Figs. 14(g) with 14(a), we can see that the NLR-PCATLC can effectively reduce isolated error points that are caused by the speckle noise, which once again validates the advantages of the NLR model.

Fig. 15 shows the CD maps of different methods on the Yellow River dataset, and Table VI lists the corresponding values of evaluation criteria. It should be noted that the noise level of the original multitemporal images is quite different. The image acquired in 2008 is a four-look image, while the image acquired in 2009 is single-look image. This means that the influence of speckle noise on the latter is much greater

TABLE V
QUANTITATIVE MEASURES ON THE ITALY DATASET

Methods	FN	FP	OE	PCC(%)	Kappa
PCA-KM	**103**	2980	3083	95.30	0.5850
MRFFCM	568	1501	1619	97.53	0.6896
NR-ELM	**195**	2123	2318	96.46	0.6462
GaborTLC	364	**402**	**766**	**98.83**	**0.8405**
PCANet	207	2298	2505	96.78	0.6262
CWNN	210	3718	3928	94.01	0.5097
NLR-PCATLC	550	**203**	**753**	**98.85**	**0.8520**

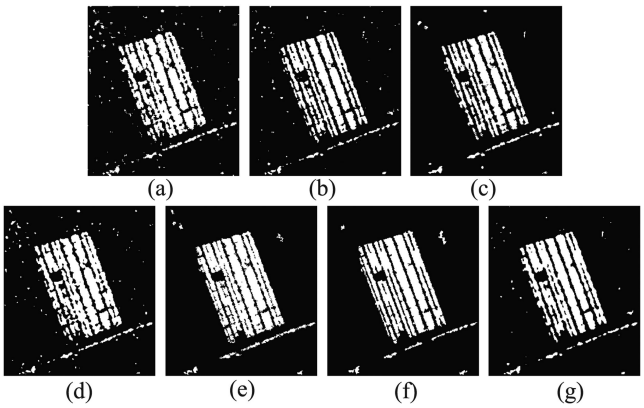

Fig. 15. Final CD maps of Yellow River dataset generated by: (a) PCA-KM; (b) MRFFCM; (c) NR-ELM; (d) GaborTLC; (e) PCANet; (f) CWNN; and (g) proposed NLR-PCATLC.

TABLE VI
QUANTITATIVE MEASURES ON THE YELLOW RIVER DATASET

Methods	FN	FP	OE	PCC(%)	Kappa
PCA-KM	2656	2149	4805	93.53	0.7784
MRFFCM	3181	**685**	3866	94.79	0.8106
NR-ELM	3570	**669**	4239	94.29	0.7897
GaborTLC	2706	1659	4365	94.12	0.7954
PCANet	**1643**	1711	**3354**	**95.48**	**0.8479**
CWNN	**1694**	712	**2406**	**96.76**	**0.8875**
NLR-PCATLC	2481	933	3414	95.40	0.8376

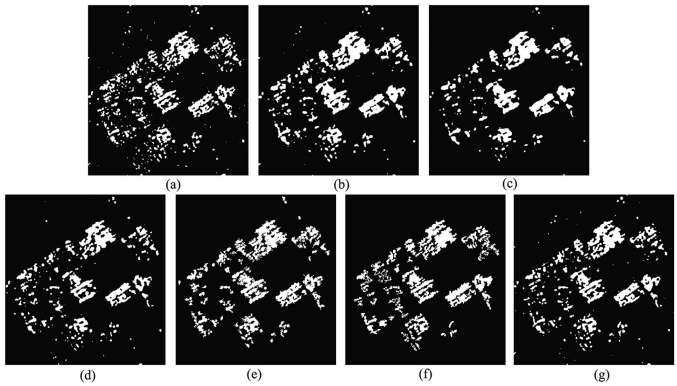

Fig. 16. Final CD maps of Yichun dataset generated by: (a) PCA-KM; (b) MRFFCM; (c) NR-ELM; (d) GaborTLC; (e) PCANet; (f) CWNN; and (g) proposed NLR-PCATLC.

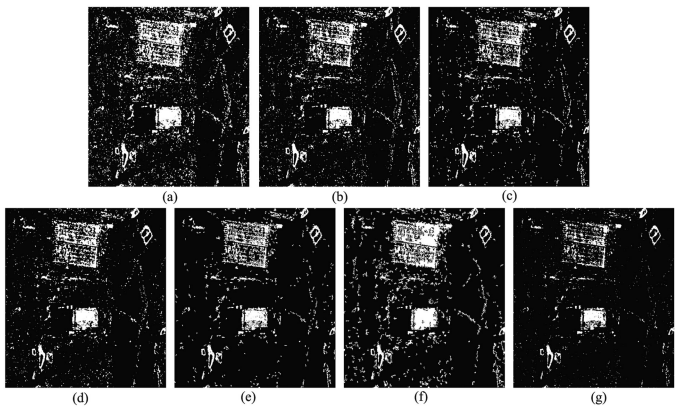

Fig. 17. Final CD maps of Wuhan dataset generated by: (a) PCA-KM; (b) MRFFCM; (c) NR-ELM; (d) GaborTLC; (e) PCANet; (f) CWNN; and (g) proposed NLR-PCATLC.

TABLE VII
QUANTITATIVE MEASURES ON THE YICHUN DATASET

Methods	FN	FP	OE	PCC(%)	Kappa
PCA-KM	2521	3670	6191	92.66	0.5860
MRFFCM	**2211**	3983	6194	92.65	0.5995
NR-ELM	2279	**2932**	5711	93.23	0.5962
GaborTLC	2935	**2821**	5756	93.17	0.5866
PCANet	2248	3721	5969	92.92	0.6078
CWNN	**2141**	3487	**5628**	**93.33**	**0.6277**
NLR-PCATLC	2337	3174	**5484**	**93.50**	**0.6264**

than the former. The huge different speckle noise level between the two multitemporal images makes the CD more complicate and difficult. According to this priori knowledge of the speckle noise, we set $L_1/L_2 = 4$ for the NLR-PCATLC. As shown in Fig. 15, the spots in NLR-PCATLC is much less than that in PCA-KM, which means that the proposed NLR-ADMM model can reduce the influence of speckle noise with different levels. On the other hand, the image details are also preserved better in the NLR-PCATLC than MRFFCM and NR-ELM. By comparing with PCA-KM, MRFFCM, NR-ELM, and GaborTLC, the NLR-PCATLC can suppress the impact of speckle noise and at the same time preserve the details that are not easy to detect. Meanwhile, it is worth noting that CWNN and PCANet on this dataset can achieve better PCC and Kappa coefficient than NLR-PCATLC, respectively. However, the time consumption of CWNN and PCANet are 832.79 and 2304.88 s for network training, respectively, which are much greater than NLR-PCATLC with 42.86 s.

Next, we test these methods on the urban building change datasets of Yichun dataset and Wuhan dataset. Their experimental results are shown in Figs. 16 and 17, and listed in Tables VII and VIII, respectively. As can be seen from the results of these comparison algorithms, their performances on the building CD are not as good as those on flood mapping tasks. This is mainly because SAR images have a lot of strong scattering points in urban areas. By comparing NLR-PCATLC with PCA-KM and GaborTLC, we can find that the proposed NLR-PCATLC can obtain cleaner results with fewer isolated error points, which can be shown in Fig. 17(a), (d), and (g). This is mainly due to its adoption of the NLR model for DI and the modified two-level clustering for classification. However, we can also find that these two steps also lead to higher false negatives, as shown in Tables VII and VIII. As can be seen from Fig. 16(f) and Table VII, the deep learning-based CWNN can achieve the best

TABLE VIII
QUANTITATIVE MEASURES ON THE WUHAN DATASET

Methods	FN	FP	OE	PCC(%)	Kappa
PCA-KM	**13691**	49066	62757	90.74	0.5438
MRFFCM	18219	31028	49247	92.73	0.5860
NR-ELM	18599	23491	42090	93.79	0.6256
GaborTLC	19054	20991	40045	94.09	0.6359
PCANet	19701	**17850**	**37551**	**94.46**	**0.6486**
CWNN	**11248**	38472	49720	92.66	0.6170
NLR-PCATLC	25918	**5960**	**31878**	**95.30**	**0.6532**

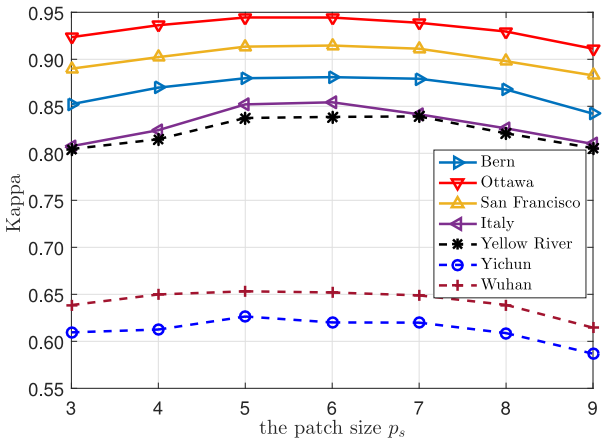

Fig. 18. CD performance comparison with different patch sizes p_s.

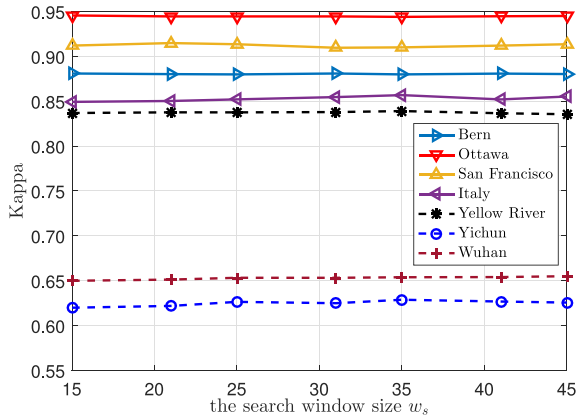

Fig. 19. CD performance comparison with different search window sizes w_s.

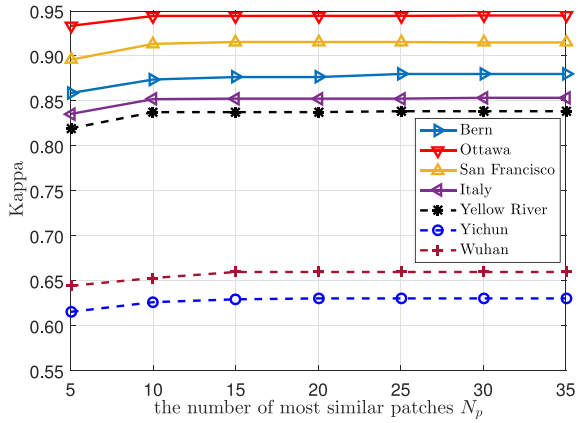

Fig. 20. CD performance comparison with different numbers of most similar patches N_p.

performance in terms of visual effect and the optimal Kappa coefficient 0.6277 on Yichun dataset, which is better than 0.6264 of NLR-PCATLC. From the above experiments, we can find that NLR-PCATLC is a quite competitive methods for SAR image CD.

4) Parameter Analysis: The last experiment is a test of parameters used in the NLR-PCATLC, which consists of two main categories: the parameters used in NLR-ADMM and PCA feature extraction. The main parameters of NLR-ADMM are the patch size p_s, the search window size w_s, and the number of most similar patches N_p. To measure the impact of these parameters, we analyze the influence of them using the above datasets. The Kappa coefficient is adopted to evaluate the detection results, which can describe the global performance of the CD. In Fig. 18, we vary the patch size p_s from 3 to 9 with step one and keep other parameters fixed as $w_s = 25$ and $N_p = 10$. It can be found that the patch size has an important impact on the CD performance. As the p_s increases, the Kappa value first grows and then drops, which is because that a too small p_s is not robust to the speckle noise, whereas a too large p_s makes it very hard to find enough similar patches. Obviously, setting $p_s = 5$ is a good choice. In Fig. 19, we vary the search window size w_s from 15 to 45 and keep other parameters fixed as $p_s = 5$ and $N_p = 10$. It can be observed that the NLR-ADMM is not quite sensitive to w_s, because the Kappa value changes only slightly as shown in Fig. 19. There are two main reasons for this: first, due to the spatial correlation of pixels and local similarity of patches, most patches can find enough similar patches to satisfy the low-rank property for the denoising within a suitable local search window, whose size w_s does not need to be very large, although a larger w_s may bring more similar patches; second, this NLR recovery process for DI generation is one step of the whole CD algorithm, a very small change in the DI may have little effect on the whole detection algorithm. Then, we can set $w_s = 25$ as a compromise choice, which can ensure that we can select enough similar patches. At last, we vary the number of most similar patches N_p from 5 to 35 with step 5 and keep other parameters fixed as $p_s = 5$ and $w_s = 25$ in Fig. 20. We can find that it can achieve a stable enough good result when $N_p = 10$. Although a large N_p can bring a better performance than a small N_p in terms of Kappa, it requires a higher computational complexity for a large N_p. Considering the CD performance and the computational costs, we empirically set $N_p = 10$. On the other hand, the main parameters of PCA feature extraction are the feature vector size s and image block size h. As stated in [25], there is no significant change in CD performance with respect to s when $3 \leq s \leq h^2$. Then, we set s equal to h for convenience in PCA feature extraction. The parameter h defines the local neighborhood size so that it affects the contribution of spatial contextual information on the feature extraction. Obviously, a large h will smoothen the effect of noise and reduce the false detections, but it will bring more miss detections, and vice versa, which has also been demonstrated by many experiments in [25]. Meanwhile, we use a rotationally symmetric Gaussian low-pass filter $\mathbf{G}$ of size 3×3

with standard deviation 0.5 in the modified two-level clustering for calculating the weighted distance maps $\mathbf{d}^c$ and $\mathbf{d}^u$. We can also choose other rotationally symmetric Gaussian low-pass filter $\mathbf{G}$ with different sizes $g_s \times g_s$ and standard deviations σ. Intuitively, this Gaussian weighted distance can be seen as a Gaussian smoothing process, which can reduce the isolated error points. The first parameter g_s, which determines the size of the neighborhood, should be considered, and the second parameter σ determines the smoothness of the matrix $\mathbf{G}$: the larger the σ, the smoother the result. In our algorithm, we empirically set $g_s = 3$ and $\sigma = 0.5$.

C. Complexity Analysis

The main computational complexity of NLR-PCATLC is concentrating on the process of NLR-ADMM (Algorithm 1).

1) Calculating the similarity metric and grouping similar patches. For each target patch, calculating the similarity $\tilde{S}_{m,n}$ in (7) requires $\mathcal{O}(p_s^2 w_s^2)$. Thus, locating the similar nonlocal neighbors for all target patches requires $\mathcal{O}(p_s^2 w_s^2 M)$, where M stands for the pixel number in the image.
2) Updating $\mathbf{z}^{k+1}$. Since SVD is required to compute (14), the complexity of updating each $\mathbf{z}_i^{k+1}$ is $\mathcal{O}(r p_s^2 N_p)$, where r represents the rank of matrix $[\mathbf{R}_i(\tilde{\mathbf{X}}_1^k - \tilde{\mathbf{X}}_2^k) + \frac{\mathbf{u}_i^k}{\rho}]$. Then, updating $\mathbf{z}^{k+1}$ requires $\mathcal{O}(r p_s^2 N_p M)$.
3) Applying the Newton method to update $\tilde{\mathbf{X}}_1^{k+1}$ and $\tilde{\mathbf{X}}_2^{k+1}$. As the linearize inexact approximation is employed in the $\tilde{\mathbf{X}}_1^{k+1}$ and $\tilde{\mathbf{X}}_2^{k+1}$ updating process, the Newton iteration in (19) and (21) only require a pointwise division, which greatly reduces the computational complexity. Therefore, updating $\tilde{\mathbf{X}}_1^{k+1}$ and $\tilde{\mathbf{X}}_2^{k+1}$ requires $\mathcal{O}(2 i_N M)$, where i_N is the iteration number of the Newton method (it is set to be five in the experiment).

In our experiment, the computational time of NLR-PCATLC on Bern, Ottawa, San Francisco, Italy, Yellow River, Yichun, and Wuhan datasets are 53.02, 59.82, 36.44 38.55, 42.86, 52.45, and 596.28 s, respectively. Although this method is obviously faster than the deep learning-based PCANet and CWNN, it is still slower than other four comparing methods. However, the NLR-PCATLC can be accelerated by several strategies. The low-rank matrix recovery can be speeded up by using the fast randomized singular value thresholding algorithm [40]. In addition, grouping similar patches and updating $\mathbf{z}^{k+1}$ can be implemented in parallel as they are independently carried out for each target patch.

D. Discussion

From the algorithmic flow of the proposed NLR-PCATLC and the experiment results, we can find that there are still some shortcomings in this algorithm. The first is its high complexity as we analyzed above, the second is that it faces great difficulties in urban CD, as shown in Figs. 16 and 17. The main reason is that it ignores the strong scattering properties of buildings, vehicles, and other objects in urban areas, which means that it still only treats the SAR image as a general natural image with multiplicative speckle noise. Therefore, the algorithm can achieve good results in the relatively easy flood detection tasks, but not so good in urban area CD. In the future, we will consider incorporating scattering information into the process of CD to improve the detection efficiency, such as the scattering characteristics of built-up areas [41], so that the application of the algorithm will be more extensive. In addition, it can be found that the DI generation process (NLR-ADMM) and the change map generation process (PCATLC) are separated from each other, which means that they are executed sequentially and performed only once. Inspired by the recently proposed method in [42], which introduces an iterative feedback-based process in the CD for flood mapping in SAR images and obtains effective performance, we can also employ the iterative feedback idea in NLR-PCATLC to fuse the DI generation and change map generation. For example, after the initial class Ω_m is obtained by FCM in (26), we can use this to update the model (9) by replacing λ with λ_i according to the clustering information, which is also our next work.

IV. Conclusion

In this article, we present a new SAR image CD method named as NLR-PCATLC for short. First, this proposed method uses the NLR model to generate the DI, which constructs a PGM for each pixel with some similar patches based on the similarity metric for the logarithmic SAR image. Then, a new low-rank minimization model based on the statistical distribution of speckle noise in two original multitemporal images is proposed, which contains a data fidelity term and a regularization term. To solve this minimization problem, the NLR-ADMM is developed by employing the ADMM framework to separate it into two subproblems, one can be solved by the WNN method, the other can be efficiently solved by the linearize approximation and Newton method. Second, with the NLR-ADMM produced DI, the PCATLC is used to extract the feature and obtain the classification result. To efficiently identify the changed class from the unchanged class, a modified two-level clustering method is proposed. It implements the FCM as the first-level clustering and uses the nearest distance criterion as the second-level clustering, which utilizes the neighbor information with Gaussian weighting to reduce the outliers. Experiments with different datasets demonstrate the effective performance of the proposed NLR-PCATLC. It can reduce the speckle influence and at the same time preserve the details. However, there are two drawbacks of proposed method that it is time-consuming on the NLR-ADMM and not so satisfactory in urban area CD. Our future work is to develop the fast algorithm of this method and integrate scattering information into the process of CD.

Acknowledgment

The authors would like to thank Prof. HengChao Li of Southwest Jiaotong University for providing the codes of GaborTLC [26]. The authors would also like to thank the editors and anonymous reviewers for their careful reading of an earlier version of this article and constructive suggestions that improved the presentation of this work.

REFERENCES

[1] Y. Ban and O. A. Yousif, "Multitemporal spaceborne SAR data for urban change detection in China," *IEEE J. Sel. Topics Appl. Earth Observ. Remote Sens.*, vol. 5, no. 4, pp. 1087–1094, Aug. 2002.

[2] J. L. Gil-Yepes, L. A. Ruiz, J. A. Recio, A. Balaguer-Beser, and T. Hermosilla, "Description and validation of a new set of object-based temporal geostatistical features for land-use/land-cover change detection," *ISPRS J. Photogrammetry Remote Sens.*, vol. 121, pp. 77–91, Nov. 2016.

[3] F. Bovolo, C. Marin, and L. Bruzzone, "A hierarchical approach to change detection in very high resolution SAR images for surveillance applications," *IEEE Trans. Geosci. Remote Sens.*, vol. 51, no. 4, pp. 2042–2054, Apr. 2013.

[4] Y. Li, M. Gong, L. Jiao, L. Li, and R. Stolkin, "Change-detection map learning using matching pursuit," *IEEE Trans. Geosci. Remote Sens.*, vol. 53, no. 8, pp. 4712–4723, Aug. 2015.

[5] Y. Yuan, H. Lv, and X. Lu, "Semi-supervised change detection method for multi-temporal hyperspectral images," *Neurocomputing*, vol. 148, pp. 363–375, Jan. 2015.

[6] M. Roy, S. Ghosh, and A. Ghosh, "A neural approach under active learning mode for change detection in remotely sensed images," *IEEE J. Sel. Topics Appl. Earth Observ. Remote Sens.*, vol. 7, no. 4, pp. 1200–1206, Apr. 2014.

[7] G. Moser and S. B. Serpico, "Unsupervised change detection from multichannel SAR data by Markovian data fusion," *IEEE Trans. Geosci. Remote Sens.*, vol. 47, no. 7, pp. 2114–2128, Jul. 2009.

[8] S. Gao, Y. Cheng, and Y. Zhao, "Unsupervised change detection of satellite images using low rank matrix completion," *Opt. Lett.*, vol. 38, no. 23, pp. 5146–5149, Dec. 2013.

[9] L. Bruzzone and D. F. Prieto, "An adaptive semiparametric and context-based approach to unsupervised change detection in multitemporal remote-sensing images," *IEEE Trans. Image Process.*, vol. 11, no. 4, pp. 452–466, Apr. 2002.

[10] F. Bovolo and L. Bruzzon, "A detail-preserving scale-driven approach to change detection in multitemporal SAR images," *IEEE Trans. Geosci. Remote Sens.*, vol. 43, no. 12, pp. 2963–2972, Dec. 2005.

[11] J. Inglada and G. Mercier, "A new statistical similarity measure for change detection in multitemporal SAR images and its extension to multiscale change analysis," *IEEE Trans. Geosci. Remote Sens.*, vol. 45, no. 5, pp. 1432–1445, May 2007.

[12] J. Ma, M. Gong, and Z. Zhou, "Wavelet fusion on ratio images for change detection in SAR images," *IEEE Geosci. Remote Sens. Lett.*, vol. 9, no. 6, pp. 1122–1126, Nov. 2012.

[13] M. Gong, Z. Zhou, and J. Ma, "Change detection in synthetic aperture radar images based on image fusion and fuzzy clustering," *IEEE Trans. Image Process.*, vol. 21, no. 4, pp. 2141–2151, Apr. 2012.

[14] W. Yan, S. Shi, L. Pan, G. Zhang, and L. Wang, "Unsupervised change detection in SAR images based on frequency difference and a modified fuzzy c-means clustering," *Int. J. Remote Sens.*, vol. 39, no. 10, pp. 3055–3075, 2018.

[15] B. Hou, Q. Wei, Y. Zheng, and S. Wang, "Unsupervised change detection in SAR image based on Gauss-log ratio image fusion and compressed projection," *IEEE J. Sel. Topics Appl. Earth Observ. Remote Sens.*, vol. 7, no. 8, pp. 3297–3317, Aug. 2014.

[16] Y. Zheng, L. Jiao, H. Liu, B. Hou, and S. Wang, "Unsupervised saliency-guided SAR image change detection," *Pattern Recognit.*, vol. 61, pp. 309–326, Jan. 2017.

[17] Y. Zhang, S. Wang, C. Wang, J. Li, and H. Zhang, "SAR image change detection using saliency extraction and shearlet transform," *IEEE J. Sel. Topics Appl. Earth Observ. Remote Sens.*, vol. 11, no. 12, pp. 4701–4710, Dec. 2018.

[18] H. Li, M. Gong, Q. Wang, J. Liu, and L. Su, "A multiobjective fuzzy clustering method for change detection in SAR images," *Appl. Soft Comput.*, vol. 46, pp. 767–777, Sep. 2016.

[19] X. Zhou, C. Yang, H. Zhao, and W. Yu, "Low-rank modeling and its applications in image analysis," *ACM Comput. Surveys*, vol. 47, no. 2, pp. 36, Jan. 2015.

[20] T. Huang, W. Dong, X. Xie, G. Shi, and X. Bai, "Mixed noise removal via Laplacian scale mixture modeling and nonlocal low-rank approximation," *IEEE Trans. Image Process.*, vol. 26, no. 7, pp. 3171–3186, Jul. 2017.

[21] K. Chang, P. Ding, and B. Li, "Compressive sensing reconstruction of correlated images using joint regularization," *IEEE Signal Process. Lett.*, vol. 23, no. 4, pp. 449–453, Apr. 2016.

[22] G. Chen, G. Li, Y. Liu, X. Zhang, and L. Zhang, "SAR image despeckling by combination of fractional-order total variation and nonlocal low rank regularization," in *Proc. IEEE Int. Conf. Image Process.*, Sep. 2017, pp. 3210–3214.

[23] D. Guan, D. Xiang, X. Tang, and G. Kuang, "SAR image despeckling based on nonlocal low-rank regularization," *IEEE Trans. Geosci. Remote Sens.*, vol. 57, no. 6, pp. 3472–3489, Jun. 2019.

[24] L. Liu, Z. Jia, J. Yang, and N. K. Kasabov, "SAR image change detection based on mathematical morphology and the K-means clustering algorithm," *IEEE Access*, vol. 7, pp. 43970–43978, 2019.

[25] T. Celik, "Unsupervised change detection in satellite images using principal component analysis and k-means clustering," *IEEE Geosci. Remote Sens. Lett.*, vol. 6, no. 4, pp. 772–776, Oct. 2009.

[26] H. C. Li, T. Celik, N. Longbotham, and W. J. Emery, "Gabor feature based unsupervised change detection of multitemporal SAR images based on two-level clustering," *IEEE Geosci. Remote Sens. Lett.*, vol. 12, no. 12, pp. 2458–2462, Dec. 2015.

[27] J. A. Hartigan and M. A. Wong, "Algorithm AS 136: A k-means clustering algorithm," *J. Roy. Statist. Soc. C-Appl.*, vol. 28, no. 1, pp. 100–108, 1979.

[28] J. C. Bezdek, *Pattern Recognition with Fuzzy Objective Function Algorithms.* Norwell, MA, USA: Kluwer, 1981.

[29] S. Krinidis and V. Chatzis, "A robust fuzzy local information C-means clustering algorithm," *IEEE Trans. Image Process.*, vol. 19, no. 5, pp. 1328–1337, May 2010.

[30] M. Gong, L. Su, M. Jia, and W. Chen, "Fuzzy clustering with a modified MRF energy function for change detection in synthetic aperture radar images," *IEEE Trans. Fuzzy Syst.*, vol. 22, no. 1, pp. 98–109, Feb. 2014.

[31] S. Gu, L. Zhang, W. Zuo, and X. Feng, "Weighted nuclear norm minimization with application to image denoising," in *Proc. IEEE Conf. Comput. Vis. Pattern Recog.*, Jun. 2014, pp. 2862–2869.

[32] C. Oliver and S. Quegan, *Understanding Synthetic Aperture Radar Images*. Rijeka, Croatia: SciTech, 2004.

[33] H. Xie, L. E. Pierce, and F. T. Ulaby, "Statistical properties of logarithmically transformed speckle," *IEEE Trans. Geosci. Remote Sens.*, vol. 40, no. 3, pp. 721–727, Mar. 2002.

[34] C. A. Deledalle, L. Denis, and F. Tupin, "Iterative weighted maximum likelihood denoising with probabilistic patch-based weights," *IEEE Trans. Image Process.*, vol. 18, no. 12, pp. 2661–2672, Dec. 2009.

[35] S. Gu, Q. Xie, D. Meng, W. Zuo, X. Feng, and L. Zhang, "Weighted nuclear norm minimization and its applications to low level vision," *Int. J. Comput. Vis.*, vol. 121, no. 2, pp. 183–208, Jan. 2017.

[36] H. Feng, B. Hou, and M. Gong, "SAR image despeckling based on local homogeneous-region segmentation by using pixel-relativity measurement," *IEEE Trans. Geosci. Remote Sens.*, vol. 49, no. 7, pp. 2724–2737, Jul. 2011.

[37] F. Gao, J. Dong, B. Li, Q. Xu, and C. Xie, "Change detection from synthetic aperture radar images based on neighborhood-based ratio and extreme learning machine," *J. Appl. Remote Sens.*, vol. 10, no. 4, Dec. 2016, Art. no. 046019.

[38] F. Gao, J. Dong, B. Li, and Q. Xu, "Automatic change detection in synthetic aperture radar images based on PCANet," *IEEE Geosci. Remote Sens. Lett.*, vol. 13, no. 12, pp. 1792–1796, Dec. 2016.

[39] F. Gao, X. Wang, Y. Gao, J. Dong, and S. Wang, "Sea ice change detection in SAR images based on convolutional-wavelet neural networks," *IEEE Geosci. Remote Sens. Lett.*, vol. 16, no. 8, pp. 1240–1244, Aug. 2019.

[40] T.-H. Oh, Y. Matsushita, Y.-W. Tai, and I. S. Kweon, "Fast randomized singular value thresholding for nuclear norm minimization," in *Proc. IEEE Conf. Comput. Vis. Pattern Recog.*, Jun. 2015, pp. 4484–4493.

[41] S. Quan, B. Xiong, D. Xiang, and G. Kuang, "Derivation of the orientation parameters in built-up areas: With application to model-based decomposition," *IEEE Trans. Geosci. Remote Sens.*, vol. 56, no. 8, pp. 4714–4730, Aug. 2018.

[42] M. Zhao, Q Ling, and F. Li, "An iterative feedback-based change detection algorithm for flood mapping in SAR images," *IEEE Geosci. Remote Sens. Lett.*, vol. 16, no. 2, pp. 231–235, Feb. 2019.

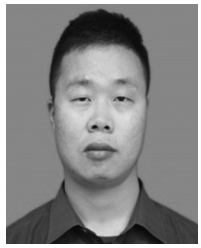

Yuli Sun received the M.S. degree from the University of Science and Technology of China, Hefei, China, in 2014. He is currently working toward the Ph.D. degree with the College of Electronic Science, National University of Defense Technology, Changsha, China, since 2019.

His research interests include machine learning and remote sensing image processing.

Lin Lei received the Ph.D. degree in information and communication engineering from the National University of Defense Technology, Changsha, China, in 2008.

She is currently an Associate Professor with the School of Electronic Science, National University of Defense Technology. Her research interests include computer vision, remote sensing image interpretation, and data fusion.

Dongdong Guan received the B.S. degree in surveying and mapping engineering from Wuhan University, Wuhan, China, in 2013, and the M.S. degree in photogrammetry and remote sensing from the National University of Defense Technology, Changsha, China, in 2015. He is currently working toward the Ph.D. degree in information and communication engineering with the College of Electronic Science, National University of Defense Technology.

His research interests include SAR image processing, machine learning, and computation vision in remote sensing applications.

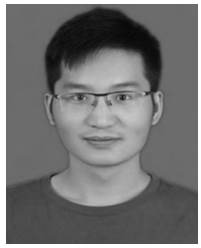

Xiao Li received the B.S. degree in the electrical engineering and automation from the University of Jinan, Jinan, China, in 2015, and the M.S. degree in control science and engineering from Xiangtan University, Xiangtan, China, in 2018. He is currently working toward the Ph.D. degree in information and communication engineering with the National University of Defense Technology, Changsha, China.

His research interests include image processing and pattern recognition, representation and dictionary learning, and computational pathology applications.

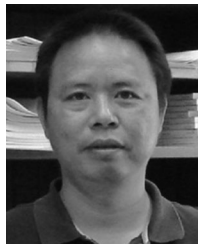

Gangyao Kuang (Senior Member, IEEE) received the B.S. and M.S. degrees in geophysics from the Central South University of Technology, Changsha, China, in 1988 and 1991, and the Ph.D. degree in communication and information from the National University of Defense Technology, Changsha, China, in 1995.

He is currently a Professor with the School of Electronic Science, National University of Defense Technology. His research interests include remote sensing, SAR image processing, change detection, SAR ground moving target indication, and classification with polarimetric SAR images.